Astronomy & Astrophysics manuscript no. scstack
January 19, 2023

Detection of intercluster gas in superclusters using the thermal Sunyaev-Zel'dovich effect

H. Tanimura[1], N. Aghanim[1], M. Douspis[1], A. Beelen[1], and V. Bonjean[1,2]

[1] Institut d'Astrophysique Spatiale, CNRS (UMR 8617), Université Paris-Sud, Bâtiment 121, Orsay, France
[2] LERMA, Observatoire de Paris, PSL Research University, CNRS, Sorbonne Universités, UPMC Univ. Paris 06, 75014, Paris, France
e-mail: hideki.tanimura@ias.u-psud.fr

ABSTRACT

Using a thermal Sunyaev-Zel'dovich (tSZ) signal, we search for the hot gas in superclusters identified in the Sloan Digital Sky Survey Data Release 7 (SDSS/DR7). We stack the Comptonization y map produced by the *Planck* Collaboration around the superclusters and detect the tSZ signal at a significance of 5.9σ. We further search for an intercluster component of gas in the superclusters. We thus remove the intracluster gas in the superclusters by masking all the galaxy groups/clusters detected by the *Planck* tSZ, *ROSAT* X-ray and SDSS optical surveys down to the total mass of 10^{13} $M_\odot$. We report the first detection of intercluster gas in the superclusters at a significance of 2.1σ. Assuming a simple, isothermal and flat density distribution of the intercluster gas over the superclusters, we estimate the product of over-density and temperature to be $\delta_e \times (T_e/8\times10^6\,\mathrm{K}) = 1.5 \pm 0.1\,(sys) \pm 0.7\,(stat)$. This can be translated as a baryon (gas) density of $(\Omega_{gas}/\Omega_b)\times(T_e/8\times10^6\,\mathrm{K}) = 0.11 \pm 0.01 \pm 0.05$. Our measurement of the intercluster gas in the superclusters may account for up to 10% of the missing baryons at low resdhifts. However, a better understanding of the physical state of the gas, especially its temperature, is required to properly estimate this contribution.

Key words. cosmology: observations – large-scale structure of Universe

1. Introduction

The formation of cosmic web structure composed of voids, filaments and clusters of galaxies is expected in the standard cosmological model of structure formation (e.g., Zeldovich et al. 1982). Superclusters of galaxies are the largest over-dense regions in the universe extending over tens of Mpc (e.g., Reisenegger et al. 2000; Batiste & Batuski 2013; O'Mill et al. 2015). Superclusters may become bound isolated structures or rather may not be gravitationally bound and split into several systems in the future (Araya-Melo et al. 2009; Chon et al. 2015). Their formation and evolution, similarly to that of the cosmic web, is governed by the dark matter and dark energy and superclusters can thus be used to test cosmological models.

Galaxies and clusters of galaxies are concentrated in superclusters and they can be identified by multiple systems of galaxy clusters or density enhancements of galaxy distribution. For example, superclusters are identified on the basis of Abell clusters (Einasto et al. 2001) and galaxy groups (Einasto et al. 2007) using smoothed density field. The friends-of-friends (FoF) method can be also used to identify superclusters from the Abell clusters (Chow-Martínez et al. 2014) and from the SDSS galaxy samples (Basilakos 2003). However, the number of known superclusters is still small at present, especially for the number of very large superclusters.

Superclusters have complex inner structures and are excellent laboratories to study the properties and evolution of galaxies and clusters of galaxies. Proust et al. (2006) suggests that intercluster galaxies in the Shapley Supercluster might contribute up to twice as much mass to the supercluster as the cluster galaxies. Furthermore, Einasto et al. (2011) shows that high-density cores of galaxy clusters are connected by galaxy chains of filaments in superclusters. However, these are based on the study with the stellar component comprising $\lesssim 10\%$ of baryons. Most of the baryons exist as a gas component, for which the distribution is unrevealed.

Especially, so-called Warm Hot Intergalactic Medium (WHIM), with a temperature range of 10^5–10^7 K (Cen & Ostriker 2006), is difficult to observe due to its low density. At high redshift ($z \gtrsim 2$), most of the expected baryons are found in the Lyα absorption forest: the diffuse, photo-ionized intergalactic medium (IGM) with a temperature of 10^4–10^5 K (e.g., Weinberg et al. 1997; Rauch et al. 1997). However, at redshifts $z \lesssim 2$, the observed baryons in stars, the cold interstellar medium, residual Lyα forest gas, OVI and BLA absorbers, and hot gas in clusters of galaxies account for only ∼50% of the expected baryons – the remainder has yet to be identified (e.g., Fukugita & Peebles 2004; Nicastro et al. 2008; Shull et al. 2012). Hydrodynamical simulations suggest that 40–50% of baryons could be in the form of shock-heated gas in a cosmic web between clusters of galaxies. Several detections in the far-UV and X-ray have been reported, but few are considered definitive (Yao et al. 2012).

Large amounts of the missing baryons may be encompassed in the crowded environment of superclusters. Especially, for the search of the elusive WHIM, the identification of the inner structures can be an effective way. Rines et al. (2001) demonstrated that Abell 2199 supercluster is kinematically connected to Abell 2197 and one or two X-ray emitting systems and identifies five X-ray faint groups between them. This may suggest the existence of intercluster gas in an extended filament between them. Moreover, Batiste & Batuski (2013) assessed the dynamics of galaxy clusters in the Corona Borealis supercluster and found that it requires substantially more mass than is contained within

the galaxy clusters by comparing with simulations, possibly indicating a significant intercluster medium contribution.

The thermal Sunyaev-Zel'dovich (tSZ) effect (Zeldovich & Sunyaev 1969; Sunyaev & Zeldovich 1970, 1972, 1980) arises from the Compton scattering of CMB photons as they pass through hot ionized gas along the line of sight. The signal provides an excellent tool for probing baryonic gas at low and intermediate redshifts. Electron pressure in the WHIM would be sufficient to generate potentially observable tSZ signals. However, the measurement is challenging due to the morphology of the source and the relative weakness of the signal. Some detection of tSZ signals from filamentary structures was reported in Planck Collaboration et al. (2013b) and Bonjean et al. (2018) and statistically by stacking methods in de Graaff et al. (2017) and Tanimura et al. (2017), but the results may be affected by the fact that properties of filaments (shape, density, temperature, etc.) are not well understood.

The *Planck* collaboration has produced a full-sky tSZ map (Comptonization y map) with 10 arcmin angular resolution and high sensitivity (Planck Collaboration et al. 2014b, 2016d). In addition to numerous galaxy clusters detected in the *Planck* data (Planck Collaboration et al. 2011a, 2014a, 2016c), the *Planck* collaboration reports the first significant tSZ signal from superclusters (Planck Collaboration et al. 2011b). With the followup study of *XMM-Newton*, PLCK G214.6+37.0 is found to be the most massive and X-ray brightest with triple systems of galaxy clusters. A cross-correlation with SDSS-DR7 Luminous Red Galaxies (LRG) and the superclusters catalogue from the SDSS-DR7 (Liivamägi et al. 2012) hinted that this triple system is encompassed in a very large–scale structure located at z ∼ 0.45 (Planck Collaboration et al. 2013a), being a part of supercluster structure. It shows that only ∼68 % of the total tSZ signal can be explained by the predictions from the X-ray signal. The discrepancy may hint to the presence of diffuse intercluster gas in the supercluster.

In this paper, we probe a hot gas in superclusters through the tSZ effect. We present the datasets used in our analysis: the SDSS DR7 supercluster catalog, *Planck* y map and several galaxy cluster catalogs to construct a mask in Section 2. In Section 3, we present the stacking method employed since the signal-to-noise ratio in the *Planck* y map is not high enough to trace superclusters individually. In Section 4, possible systematic effects and interpretations of our measurements are discussed. Finally we summarize our findings in Sect. 5. Throughout this work, we adopt a ΛCDM cosmology with the *Planck* (Planck Collaboration et al. 2016b) for conversion of redshifts into distances. R_{500} is the radius in which the mass of M_{500} is enclosed within a sphere of radius R_{500} such that the enclosed density is 500 times the critical density of the universe at redshift z.

2. Data

2.1. Planck y maps

The *Planck* tSZ map is one of the datasets provided in the *Planck* 2015 data release. It is available in HEALpix[1] format with a pixel resolution of $N_{\rm side} = 2048$. Two types of y map are publicly available: MILCA (Hurier et al. 2013) and NILC (Remazeilles et al. 2013), both of which are based on multi-band combinations of the *Planck* frequency maps (Planck Collaboration et al. 2016d). The y map produced with NILC shows a higher noise level at large scales (Planck Collaboration et al. 2016d). Such a large-scale noise can be difficult to model precisely in the stacking analysis for superclusters subtending relatively large angular scales. For this reason, we base our analysis on the *Planck* y map produced with MILCA and we check the consistency of our results with the NILC y map in Sect. 4.

The 2015 *Planck* data release also provides sky masks suitable for analyzing the y maps, including a point source mask and galactic masks that exclude 40, 50, 60 and 70% of the sky. We combine the point source mask with the 40% galactic mask which excludes ∼50% of the sky (upper panel in Fig. 2).

2.2. Supercluster catalog

The SDSS DR7 supercluster catalogue is constructed from the flux-limited samples of SDSS DR7 583,362 spectroscopic galaxies by Liivamägi et al. (2012). The superclusters are defined as over-dense regions in the luminosity density field using the B_3 spline kernel of the radius of 8 h^{-1}Mpc. Two types of thresholds are used, one with an adaptive local threshold and the other with a global threshold. We adopt the "main" catalogue of well-defined 982 superclusters with a high global threshold to study the details in the structure. The catalogue provides the position and distance of the highest density peak as its centre as well as the diameter defined by the maximum distance between its member galaxies. The centre of mass using the stellar masses of galaxies is also provided.

2.3. Catalogue of galaxy groups/clusters

We briefly present the galaxy groups/clusters catalogues used in our analysis. In order to detect the contribution from intracluster gas in superclusters to the tSZ signal, all clusters and groups from the catalogues listed below are masked in the *Planck* y map.

The *Planck* collaboration constructed a catalogue of galaxy clusters detected using the tSZ effect from the 29 month full-mission data (Planck Collaboration et al. 2016a). It contains 1653 sources, of which 1203 are confirmed clusters using multi-wavelength search for counterparts with radio, microwave, infrared, optical and X-ray data sets. The mass ($M500$) of the 1094 clusters with redshift are estimated with the SZ flux using the scaling relation $Y_{500} - M_{500}$ from Planck Collaboration et al. (2014a).

The MCXC is the catalogue of galaxy clusters based on the *ROSAT* All Sky Survey (Piffaretti et al. 2011). The MCXC comprises 1743 clusters, for which total mass (M_{500}) is estimated using the $L_{500} - M_{500}$ scaling relation from Pratt et al. (2009) as well as the radius (R_{500}), where the X-ray luminosity is corrected to the one in 0.1−2.4 keV band luminosities L_{500} by the gas density profile of Croston et al. (2008).

Tago et al. (2010) extracts 78,800 groups of galaxies from the same SDSS DR7 galaxies, used in Liivamägi et al. (2012), by adopting a modified friends-of-friends method with a slightly variable linking length. The linking length is calibrated with a flux-limited test sample. The virial radius is estimated using the projected harmonic mean of member galaxies.

Rykoff et al. (2014) introduces redMaPPer, which is a red-sequence cluster finder designed to make optimal use of large photometric surveys. They apply the redMaPPer algorithm to ∼ 10,000 deg^2 of SDSS DR8 data and present the resulting catalog of 26,111 clusters (redMaPPer catalog v6.3) over the redshift range between 0.08 and 0.55. The algorithm exhibits excellent photometric redshift performance and the richness estimates are tightly correlated with external mass proxies. We estimate the

[1] http://healpix.sourceforge.net/

mass (M_{500}) using the scaling relation of $M_{500} - \lambda$ described in Jimeno et al. (2017).

Wen et al. (2012) identify 132,684 groups and clusters using the photometric redshifts of galaxies from the SDSS DR8 data in the redshift range of 0.05 and 0.8. The catalogue has been updated with 25,419 new rich clusters at high redshift using SDSS DR12 spectroscopic data in Wen & Han (2015). To determine the mass of galaxy clusters accurately, the masses of 1191 clusters estimated by X-ray or tSZ measurements are used to calibrate the optical mass proxy, in which they find that the mass (M_{500}) is well correlated with the total luminosity (L_{500}). Using the scaling relation, the masses of all the 158,103 clusters have been updated, of which 89% have spectroscopic redshifts.

Banerjee et al. (2018) presents a galaxy cluster catalogue constructed from the SDSS DR9 data using an Adaptive Matched Filter (AMF) technique (Kepner & Kim 2000). The catalogue has 46,479 galaxy clusters with richness $\lambda 200 > 20$ in the redshift range of 0.045 and 0.641 in $\sim$ 11,500 deg^2 of the sky. The AMF algorithm identifies clusters by finding the peaks in a cluster likelihood map generated by convolving a galaxy survey with a filter based on a cluster model and a background model. In Banerjee et al. (2018), an NFW density profile and a Gaussian model for photometric redshift uncertainties for filters in position and redshift are assumed respectively. The AMF approach provides simultaneous determination of richness, core and virial radii (R_{200}), and redshift. The technique does not rely on the red sequence for cluster detection, potentially allowing for the detection of galaxy clusters that do not possess a central luminous red galaxy.

In Banerjee et al. (2018), the AMF DR9 catalogue is compared with the redMaPPer (26,350 clusters) and the WHL (132,684 clusters) in the same area of the sky and in the overlapping redshift range. The AMF DR9 matches 97% of the richest Abell clusters (Richness group 3), same as WHL, while redMaPPer matches $\sim$ 90% of these clusters. For comparisons with X-ray clusters such as MCXC and REFLEX, especially for most luminous clusters ($Lx > 8 \times 10^{44}$ ergs/sec), they find that the AMF DR9 performs equivalently to WHL for the identification of clusters.

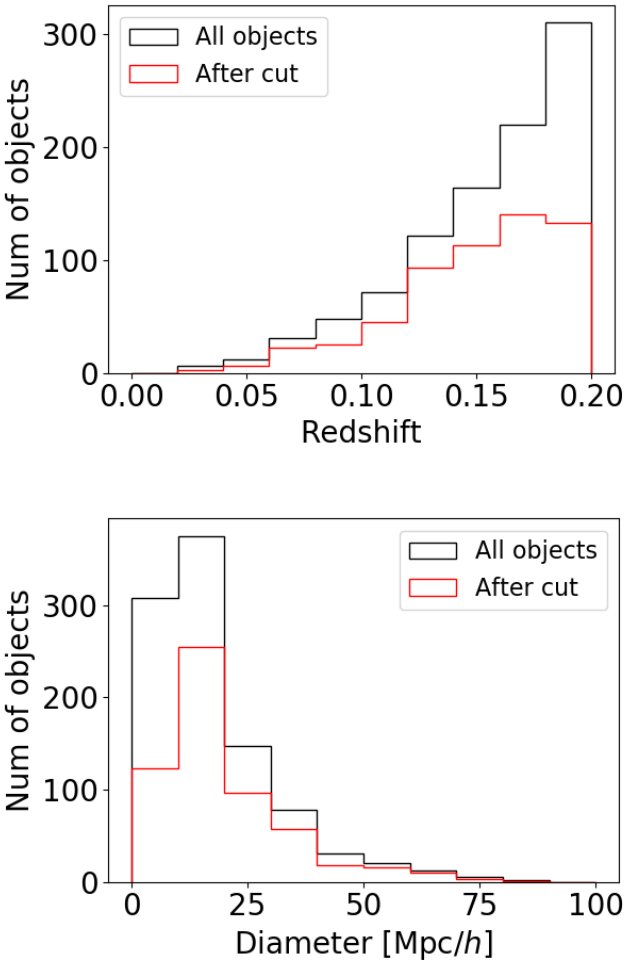

Fig. 1. *Upper*: The redshift distribution of superclusters. *Lower:* The diameter distribution of superclusters in Mpc/h. The *black* and *red* show the distributions of all the 982 superclusters in the catalogue and 580 selected ones used in the stacking analysis to probe the intercluster gas in the superclusters.

3. Analysis

3.1. Stacking y map centred on superclusters

In this section, we describe our procedure for stacking the *Planck* y map against the superclusters and construct the stacked y profile. For each supercluster, we extract the y map on the same grid in "scaled radius" in a 2-dimensional coordinate system of $-2.5 < \Delta l/\theta_{sc} < +2.5$ and $-2.5 < \Delta_b/\theta_{sc} < +2.5$ divided in 31 $\times$ 31 bins and the corresponding y profile. For each supercluster, we calculate the scaled radius using the half diameter and radial distance provided in the catalogue. The projected distances on the *Planck* y map are normalized accordingly. The mean tSZ signal in the annular region of [1.5, 5.0] $\times$ (an angular size of a supercluster) is subtracted for each supercluster as an estimate of the local background signal.

First, we stack the y map without masking the galaxy clusters (upper panel in Fig. 2). In this step, we analyse the stacked signal of a sample of 789 superclusters from the catalogue of Liivamägi et al. (2012), all laying outside the *Planck* galactic and point-source masks. The left panel in Fig. 3 shows the average stacked y map and the right panel shows the corresponding y profile with 1σ uncertainties. The uncertainties are estimated by a bootstrap resampling (see Sect. 3.4). The tSZ signal is detected at a significance of 5.9σ and is dominated by the central peak of $y \sim 2.6 \times 10^{-7}$. It indicates that the hot gas (mainly in galaxy clusters) traced by the tSZ signal is concentrated in the central positions of the superclusters, which should be in the centre of the associated gravitational potential.

Two centres are defined in the catalogue of superclusters: One using the smoothed density field of luminosities and one deduced from the stellar masses of galaxies. The stacked y profile using the mass centres is shown in the right panel of Fig. 3. Compared with the stacked y profile using the luminosity centres, one using the mass centres looks flatter. This may imply that the centres of superclusters are better defined by the luminosity centres rather than by the mass centres. Therefore, we adopt the luminosity centres for the centres of superclusters. We will discuss it more in Sect. 4.1.

3.2. Applying the mask of galaxy clusters

Now, we focus on probing the intercluster gas, located outside of galaxy clusters in the superclusters. We thus mask the groups and galaxy clusters detected in the *Planck* tSZ, *ROSAT* X-ray and SDSS optical surveys described in Sect. 2.3. We apply a galaxy-

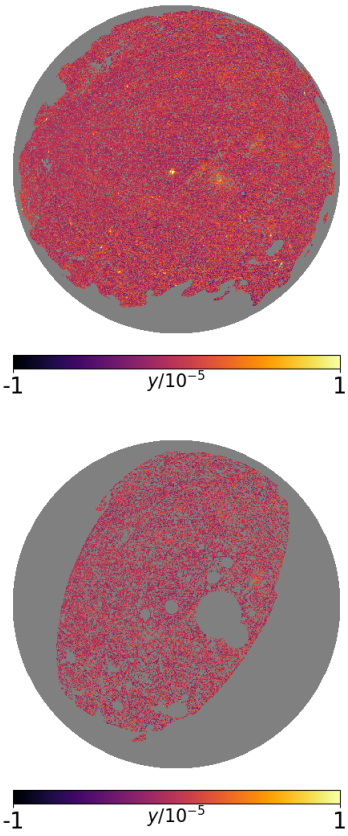

Fig. 2. *Upper*: The *Planck* y map with the 40% galactic mask and point-source mask from the view of the north galactic pole. *Lower:* The *Planck* y map after masking galaxy clusters. The galaxy groups/clusters detected by the *Planck* tSZ, *ROSAT* X-ray and SDSS optical surveys described in Sect. 2.3 are all masked by three times the radius ($3 \times R_{500}$) of each galaxy cluster. The region outside of the SDSS DR7 survey is also excluded.

cluster mask set to three times the cluster radius ($3 \times R_{500}$). For *Planck* SZ clusters without assigned radius, we mask a region of 10 arcmin in radius, corresponding to the *Planck* beam of the *Planck* y map. In addition, we remove the region outside of the SDSS DR7 survey (lower panel in Fig. 2) and we apply the mask used to produce the y map. The union mask is applied during the stacking process: for a given supercluster, masked pixels in the y map are not accumulated in the stacked image.

Due to this mask, some superclusters are largely masked and may bias our results. Therefore, we remove from our analysis for superclusters if 40% of the region or more than $\sim 0.3 \times 0.3$ deg^2 in the superclusters is not available. Here again, superclusters laying at the boundary of the SDSS survey area are discarded from the analysis. We finally perform the stacking on the remaining 580 superclusters.

The lower panel in Fig. 2 shows the y map we use to probe the intercluster gas. As an example, one supercluster is shown before masking the galaxy clusters and after masking them in Fig. 4. Without the mask, bright signals from galaxy clusters are seen especially around the core, but they are well covered by the mask.

We check the effect of masking the galaxy clusters. In Fig. 5, the stacked y maps and the corresponding y profiles using three different sizes of masks are compared. We mask clusters using a radius of $2 \times R_{500}$ (*left*), $3 \times R_{500}$ (*middle*) and $4 \times R_{500}$ (*right*). The bright central peaks associated with the clusters disappear in all the cases, showing that the masks work well to remove the signal from galaxy clusters. However, a slight difference is seen. A residual around the core may remain in the left panel. While a slight excess around the centre would be expected since this is a 2D-projection of a 3D structure with a over-dense region around the core, it is better suppressed in the middle and right panel. On the other hand, bright spots re-appear in the right panel even with a larger-sized mask. It shows that the noise starts to dominate due to too large a mask (i.e. less regions available for the stacking). Therefore, we adopt a size of $3 \times R_{500}$ for the mask of galaxy clusters. With this mask, the average tSZ signal "outside of the mask" in the superclusters is found to be $y = 3.3 \times 10^{-8}$.

3.3. Signal-to-noise ratio

We assess the signal-to-noise (S/N) ratio of the tSZ signal from the superclusters. The S/N ratio for one supercluster can be estimated as the ratio of the mean y amplitude in a supercluster to the *rms* fluctuation in its background. The average S/N ratios of the 580 superclusters is ~ 0.8. For the stacked superclusters, we assess the S/N ratio of our measurement (Sect. 3.2) from the stacked y map and find it to be $S/N = 2.1$.

3.4. Null tests and error estimates

To assess the significance of the signal and estimate its uncertainty, we perform a Monte Carlo-based null test. We move the centre of each supercluster by a random angle in galactic longitude (while keeping the galactic latitude fixed, to avoid any systematic galactic background signal). For example, the centre of one supercluster is changed from [galactic longitude, galactic latitude] = [10°, 60°] to [150°, 60°]. We then stack the y map at the new "random" positions of superclusters, and we repeat the stacking process of the full samples 1000 times to determine the *rms* fluctuations in the background (and foreground) sky. Fig. 6 shows one of the 1000 stacked y maps: the map has no discernible structure. We can use this ensemble of maps to estimate the uncertainty of the signal quoted above. We find that the ensemble of maps has a mean and standard deviation of $y = (0.0 \pm 1.4) \times 10^{-8}$ in Fig. 7. Since the average signal in this null-test set of maps is consistent with zero, we infer that our estimator is unbiased. Our measurement results in $y = (3.3 \pm 1.4) \times 10^{-8}$ at a significance of 2.3σ.

We also assess the significance of our measurement by a bootstrap resampling. For this, we draw a random sampling of 580 superclusters (789 before masking groups and clusters) with replacement and re-calculate the average y value for the new set of 580 superclusters. We repeat this process 1000 times and the bootstrapped data produce 1000 average y values. Their average and *rms* fluctuation are $y = (3.3 \pm 1.4) \times 10^{-8}$ at a significance of 2.3σ, which is consistent with the error estimate from the null test.

3.5. Likelihood of y profile to null hypothesis

From the null-test set of maps described above, we can generate an ensemble of 1000 null y profiles and construct their covariance matrix to estimate the uncertainties of the data y profile. We can assess the likelihood of the measured y profile to the null hypothesis with the chi-square test by computing

$$\chi^2 = \sum_{i,j} (y(\theta_i) - y_{mod}(\theta_i))^T (C^{-1})_{ij} (y(\theta_j) - y_{mod}(\theta_j)), \qquad (1)$$

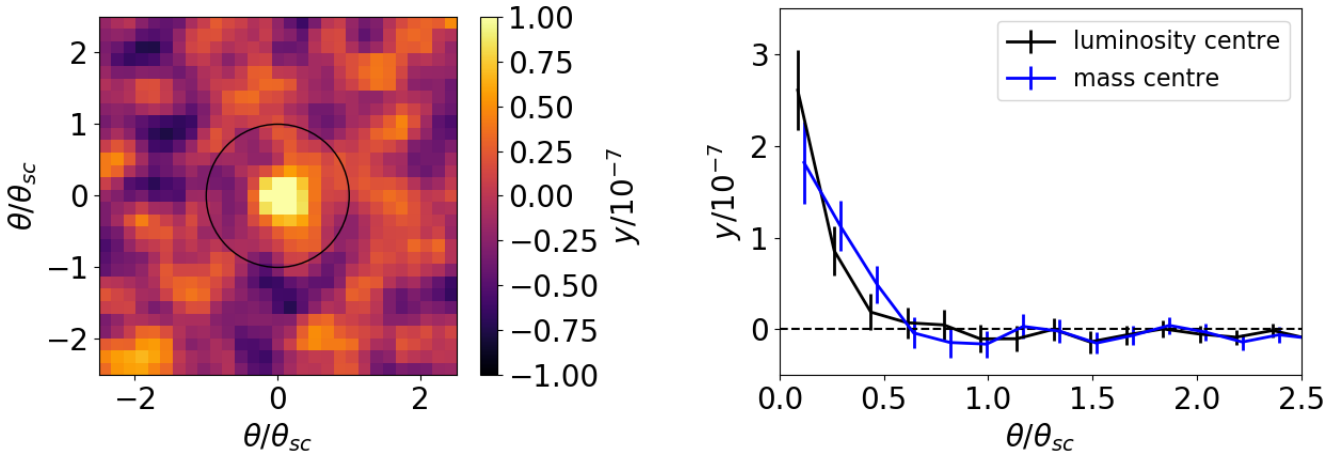

Fig. 3. *Left*: The average *Planck* y map stacked against 789 superclusters in a coordinate system where the superclusters are located at the centre and the sizes are normalized to one. For the centres of superclusters, the luminosity centres are used. The square region, $-2.5 < \Delta l/\theta_{sc} < +2.5$ and $-2.5 < \Delta_b/\theta_{sc} < +2.5$, comprises 31×31 pixels. The *black* circle represents the boundary of the superclusters assuming their circular shapes. *Right*: The corresponding radial y profile (*black*) is compared with the y profile using the mass centres (*blue*). The 1σ uncertainties are estimated by a bootstrap resampling respectively (see Sect. 3.4).

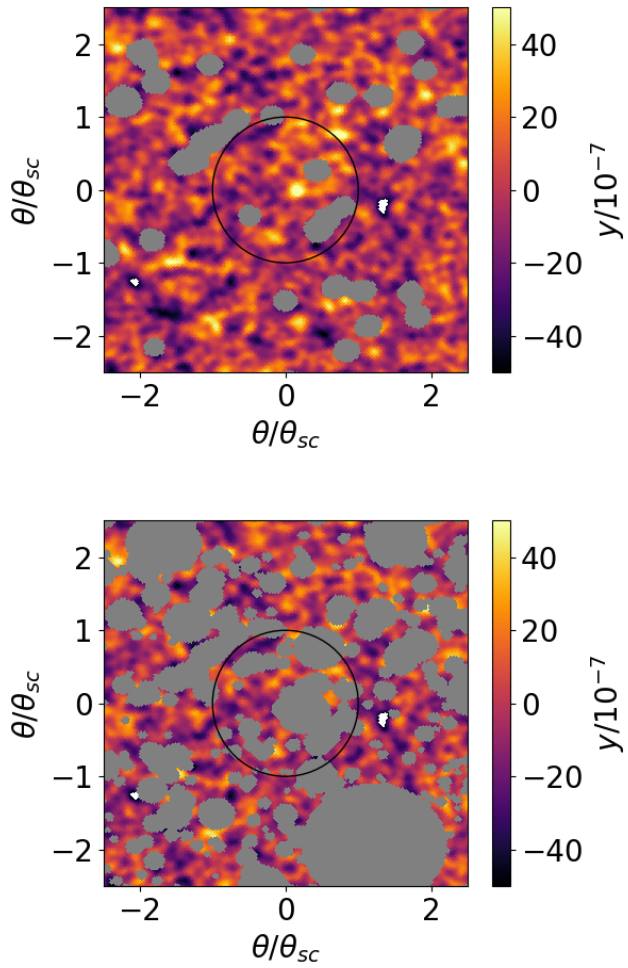

Fig. 4. The y map around one supercluster before masking galaxy clusters (*upper*) and after masking them (*lower*). The mask size is set to be three times the radius ($3 \times R_{500}$) of galaxy clusters.

where $y(\theta_i)$ is the y value at i-th angular bin from the data and $y_{mod}(\theta_i)$ is the corresponding value for a model ($y_{mod}(\theta_i) = 0$ for the null hypothesis). We verity that the χ^2 distribution for the 1000 null-test sample is well described by a chi-squared distribution with 11 degrees of freedom (11 data points up to the scaled radius of ~ 1.8) in Fig. 8. The χ^2 value of the data y profile to the null hypothesis is estimated to be 22.8 for $dof = 11$, providing a probability-to-exceed (PTE) of 0.018 which translates into a significance of 2.3σ.

We calculate the covariance matrix of the y profile in each radial bin from the 1000 average y profiles obtained from the bootstrap resampling (see Sect. 3.4). Using this covariance matrix, we calculate the likelihood of the data y profile to the null hypothesis to be PTE = 0.035 which translate into a significance of 2.1σ. We adopt this covariance matrix to estimate the final uncertainty of the mean y profile due to instrumental noise and sky noise (i.e., cosmic variance and background subtraction errors).

4. Interpretation

4.1. Systematic errors

We explore potential systematic effects in the measurement due to the *Planck* beam. Indeed the *Planck* beam may dilute the amplitude of y-value in the superclusters in Fig. 3. However, the mean angular size of the superclusters is ~ 2.8 deg and it should be a minor effect compared to the effective *Planck* beam in the y map of 10 arcmin. Second, the intercluster gas in the superclusters may be due to beam-convolution of tSZ signal from galaxy clusters inside the supercluster. While this "leakage" must be present at some level, if it were the dominant explanation for the residual signal, we would expect a significance difference for different sizes of cluster masks. However, the fact that we see no significant difference suggests that the contribution from the leakage is not significant. We also check the effect of using the two *Planck* y maps, MILCA and NILC, and find a consistent result, however, with a slight offset in Fig. 9. We will discuss it more in Sect. 4.2.

As discussed in Sect. 3.1, two types of centers are defined for the superclusters using luminosities and stellar masses of galax-

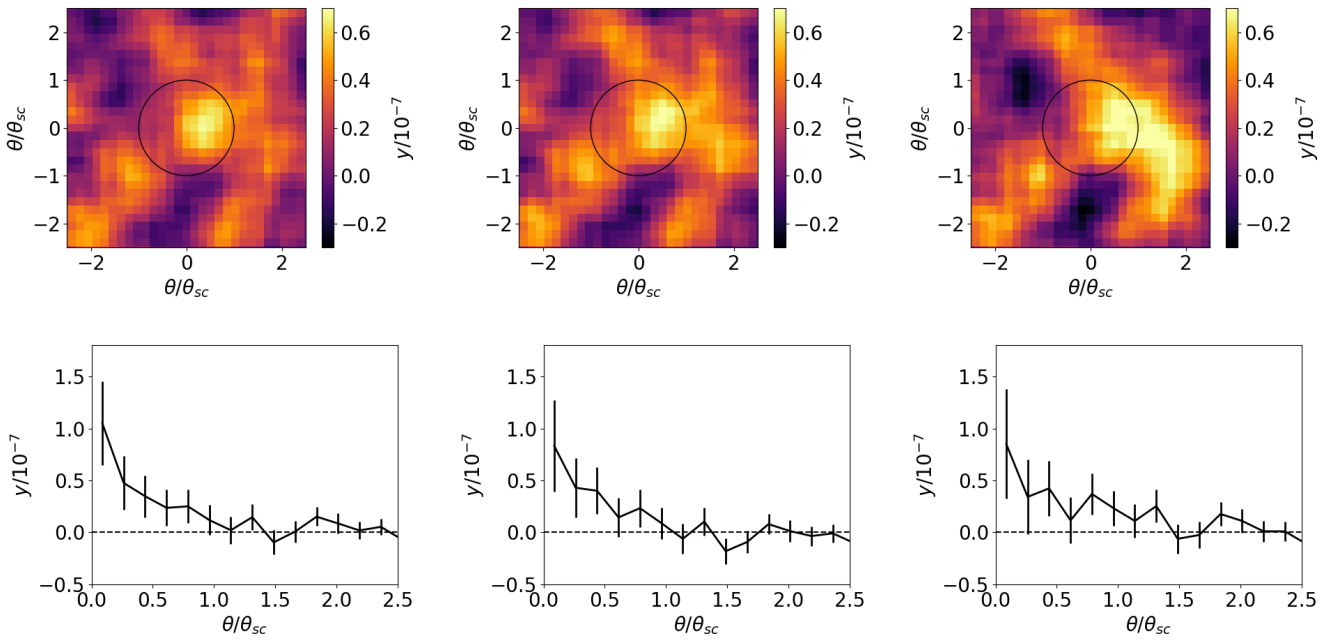

Fig. 5. The stacked y maps and corresponding y profiles using different sizes of masks for galaxy clusters: $2 \times R_{500}$ (*left*), $3 \times R_{500}$(*middle*) and $4 \times R_{500}$ (*right*). In our analysis, we adopt the size of $3 \times R_{500}$ for the mask of galaxy clusters.

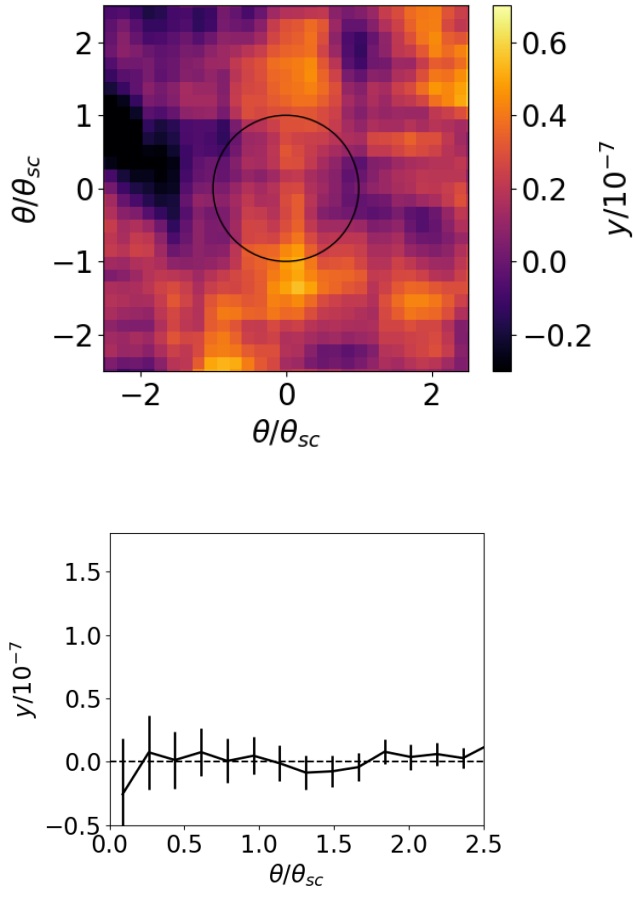

Fig. 6. *Upper*: A sample null map obtained by stacking the y map against the 580 superclusters that were moved in galactic longitude by random amounts. *Lower*: The corresponding radial y profile.

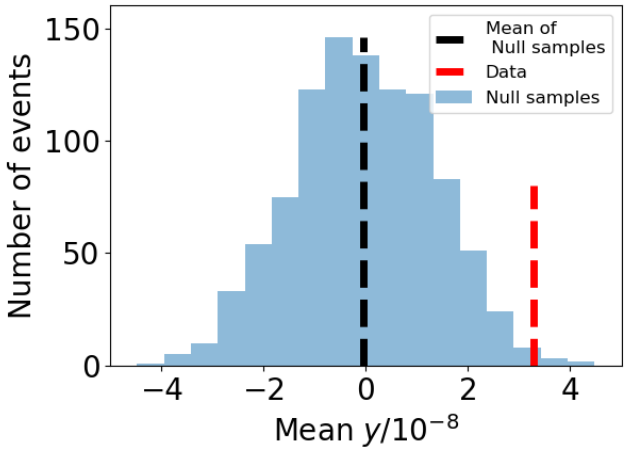

Fig. 7. The distribution of the mean y amplitude measured in 1000 null maps. The mean of the distribution is shown in *black dashed line* and the average y signal from the data is shown in *red dashed line*.

ies and we found that the stacked y profile using the mass centres is flattened compared to the one using the luminosity centres before masking galaxy clusters (see Fig. 3). A similar flattened y profile using the mass centres is also seen after masking galaxy clusters. This suggests that the luminosity centres are more appropriate definitions for the centres of supercusters. We also note that the peak in the stacked y map in Fig. 5 slightly shifts from the positions defined as the centres of superclusters. This implies that the morphologies of superclusters and hence their gas distributions are complex due to their shallow gravitational potentials.

As a matter of fact, the morphology of the SDSS superclusters was studied in Einasto et al. (2011) using ~ 35 large superclusters containing at least 300 member galaxies. The authors showed 2D and 3D distributions of galaxies and rich groups in

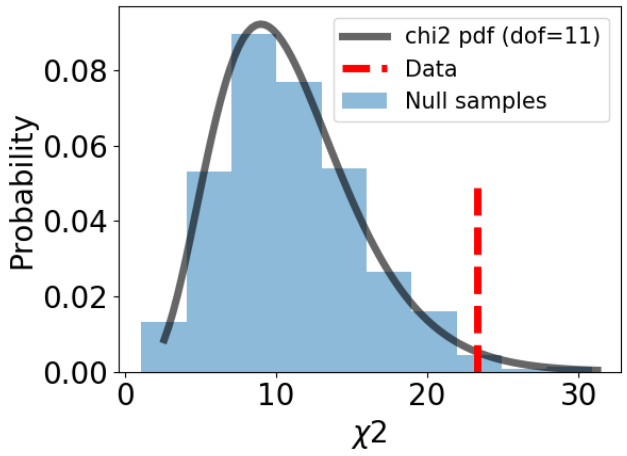

Fig. 8. The χ^2 distribution of the 1000 null samples to the null hypothesis (*blue*) is compared with the probability distribution with 11 degrees of freedom (*black*). The χ^2 value of the data y profile to the null hypothesis is shown in *red dashed line*.

the superclusters and found that most of them have filament-like overall shapes. For the filamentary superclusters, the tSZ signal would be diluted in the average y profiles. We will discuss it more in Sect. 5.

4.2. Gas properties

The Compton y parameter produced by the tSZ effect is given by

$$y = \frac{\sigma_{\rm T}}{m_{\rm e}c^2} \int n_{\rm e} k_{\rm B} T_{\rm e}\, dl, \tag{2}$$

where $\sigma_{\rm T}$ is the Thomson scattering cross section, $k_{\rm B}$ is the Boltzmann constant, $m_{\rm e}$ is the electron mass, c is the speed of light, $n_{\rm e}$ is the electron number density, $T_{\rm e}$ is the electron temperature, and the integral is taken along the radial direction. In general, the electron density at position $\mathbf{x}$ may be expressed as

$$n_{\rm e}(\mathbf{x}, z) = \overline{n}_{\rm e}(z)(1 + \delta(\mathbf{x})), \tag{3}$$

where $\delta(\mathbf{x})$ is the density contrast, and $\overline{n}_{\rm e}(z)$ is the mean electron density in the universe at redshift z,

$$\overline{n}_{\rm e}(z) = \frac{\rho_{\rm b}(z)}{\mu_{\rm e} m_{\rm p}}, \tag{4}$$

where $\rho_{\rm b}(z) = \rho_{\rm c}\Omega_{\rm b}(1+z)^3$ is the baryon density at redshift z, $\rho_{\rm c}$ is the present value of critical density in the universe, $\Omega_{\rm b}$ is the baryon density in unit of the critical density, $\mu_{\rm e} = \frac{2}{1+\chi} \simeq 1.14$ is the mean molecular weight per free electron for a cosmic hydrogen abundance of $\chi = 0.76$, and $m_{\rm p}$ is the mass of the proton.

We can estimate the physical properties of the intercluster gas we measure by considering a simple, isothermal, flat density distribution of gas (electrons) in the superclusters with spherical shapes. Under this simple model, the profile of the Compton y parameter can be expressed as a geometrical projection of a density profile with $n_{\rm e}(r, z)$

$$y(r_\perp) = \frac{\sigma_{\rm T} k_{\rm B}}{m_{\rm e}c^2} \int_{r_\perp}^{R} \frac{2r\, n_{\rm e}(r,z)\, T_{\rm e}(z)}{\sqrt{r^2 - r_\perp^2}}\, dr, \tag{5}$$

where $r_\perp$ is the tangential distance from a supercluster on the map and R is the radius of a supercluster. Assuming a negligible evolution, with a constant over-density $\delta_{\rm e}$ and constant temperature $T_{\rm e}$, of the intercluster gas in the superclusters out to $z = 0.2$ (the maximum redshift in our supercluster sample),

$$n_{\rm e}(r,z) = \frac{n_{\rm e}(r,z)\,\overline{n}_{\rm e}(z)}{\overline{n}_{\rm e}(z)} = \delta_{\rm e}\,\overline{n}_{\rm e}(z=0)\,(1+z)^3, \tag{6}$$

$$T_{\rm e}(z) = T_{\rm e}. \tag{7}$$

For this model, we fit the data y profile up to the scaled radius of 2.5 using the covariance matrix from the bootstrap resampling. We perform a nonlinear least-square fit to the data and derive a best-fit value and uncertainty on the gas over-density and temperature,

$$\delta_{\rm e} \times \left(\frac{T_{\rm e}}{8\times10^6\ {\rm K}}\right) = 1.6 \pm 0.7 \tag{8}$$

with $\chi^2/dof = 1.1$ for dof=14 (15 data point up to the scaled radius of 2.5 with one fit parameter for the amplitude of the y profile). The best-fit line is shown in Fig. 9. Assuming a gas temperature of $T_{\rm e} = 8\times10^6$ [K], which is the temperature in filaments between LRGs estimated from simulations in Tanimura et al. (2017), our result suggests that the intercluster gas spreads over the superclusters with a low density.

To investigate systematic errors on the derived value in Eq. 8, we repeat our analysis using the *Planck* NILC y map. The measured y profile agrees with the measurement using the MILCA y map with a slight offset (see Fig. 9) that lowers the derived value to 1.4 ± 0.7. We include this difference to our measurement as a systematic error, resulting in

$$\delta_{\rm e} \times \left(\frac{T_{\rm e}}{8\times10^6\ {\rm K}}\right) = 1.5 \pm 0.1\,(sys) \pm 0.7\,(stat) \tag{9}$$

that corresponds to

$$\overline{n}_{\rm e} \times \left(\frac{T_{\rm e}}{8\times10^6\ {\rm K}}\right) = (3.1 \pm 0.2\ \pm 1.4) \times 10^{-7} [/{\rm cm}^3] \tag{10}$$

for the mean electron density in the 580 superclusters.

4.3. X-ray signals

The thermal SZ effect has a linear dependence on gas density, on the other hand, the X-ray emission has a quadratic dependence. The X-ray emission is therefore important to break the degeneracy between the density and temperature. Thus, we stack the *ROSAT* X-ray count rate maps [2] around the superclusters in the same way as for the *Planck* y maps. We use the *ROSAT* maps from the total energy band (0.1-2.4 keV), hard energy band (0.5-2.4 keV), and soft energy band (0.1-0.4 keV) respectively. The galaxy clusters listed in Sect. 2.3 are all masked. We find an average X-ray signal consistent with zero. Given the constraints we found on the low density of the intercluster contribution, the result we find is expected. While the degeneracy between the density and temperature of the intercluster gas still remains, our result consistent with zero suggests that no significant signal is detected from X-ray emitting systems such as galaxy clusters which are well masked.

[2] http://www.dlr.de/dlr/en/desktopdefault.aspx/tabid-10424/

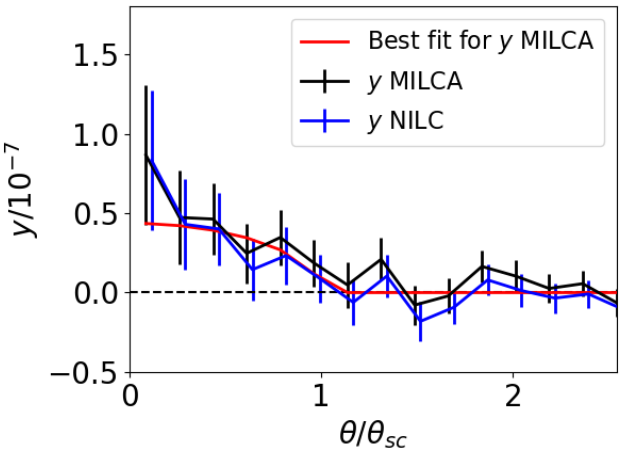

Fig. 9. The average *Planck* y profile stacked against 580 superclusters using the *Planck* MILCA (*black*) and NILC (*blue*) y map, where three times the radius ($3\times R_{500}$) of galaxy clusters are masked. The measured y profile with the MILCA y map is fitted using the model with a constant over-density and constant temperature of the gas in the superclusters, described in Sect. 4.2 (*red*).

4.4. Baryon budget of intercluster gas in superclusters

Diffuse gas in superclusters contributes to the total budget of the baryons embedded in the large-scale structure. We estimate the total amount of gas we measure using the model described in Sect. 4.2. The total mass of the gas in the 580 superclusters can be evaluated using the over-density of electrons derived in Eq. 9 assuming that the superclusters are spherically symmetric as

$$M_{gas} = \sum_{i}^{N=580} \mu_{\rm e}\, \delta_{\rm e}\, \overline{n}_{\rm e}(z)\, V(i)_{sc} \left(V(i)_{sc} = \frac{4\,\pi\, r(i)_{sc}^3}{3} \right), \quad (11)$$

where $V(i)_{sc}$ is the spherical volume of i-th supercluster using the diameter ($= 2r(i)_{sc}$) reported in the catalogue. The gas mass density can be calculated by setting

$$\rho_{gas} = \frac{M_{gas}}{V_c(z=0.2) \times f_{SDSS}}, \quad (12)$$

where $V_c(z = 0.2)$ is the comoving volume at $z = 0.2$ (the maximum redshift in the supercluster samples) and $f_{SDSS} \sim 0.2$ is the fractional SDSS-DR7 survey field on the sky. The gas mass density relative to the critical density of the universe, Ω_{gas}, can be described as

$$\left(\frac{\Omega_{gas}}{\Omega_b}\right) \times \left(\frac{T_{\rm e}}{8\times10^6\ {\rm K}}\right) = 0.11 \pm 0.01\ \pm 0.05. \quad (13)$$

Note that the derived gas mass density is inversely proportional to the temperature of the gas. For example, Werner et al. (2008) studies the gas properties in a filament connecting the massive Abell clusters A222 and A223 at redshift $z \sim 0.21$ using XMM-Newton observations and they find $kT = 0.91 \pm 0.25$ keV ($T \sim 1.1 \times 10^7$ K). With this higher temperature, the gas density can be estimated lower to be $\Omega_{gas}/\Omega_b \simeq 0.08$.

Assuming a gas temperature of $T_{\rm e} = 8 \times 10^6$ K ($\Omega_{gas}/\Omega_b \sim 0.11$), the total masses of the intercluster gas in the superclusters can be estimated to be $10^{12} - 10^{16}\ M_\odot$with its average of $10^{14.7}\ M_\odot$.

5. Discussion and conclusion

In this paper, we present the first stacking analysis of the *Planck* tSZ maps around superclusters identified by Liivamägi et al. (2012) from the SDSS DR7 galaxies. We detect the total tSZ signal from 789 superclusters at a significance of 5.9σ. This tSZ signal includes both intracluster and intercluster gas. To unveil the signal from the diffuse low-density intercluster gas, we mask the galaxy groups/clusters reported in tSZ, X-rays and optical surveys. We report the first detection of the tSZ signal from intercluster gas in the superclusters at a significance of 2.1σ. The significance was estimated from null tests and bootstrap resampling and it includes possible systematic effects in the *Planck* tSZ maps.

Assuming a simple spherical geometry, isothermal and flat density distribution of the intercluster gas in the superclusters, we estimate the product of over-density and temperature to be $\delta_e \times (T_{\rm e}/8 \times 10^6\,{\rm K}) = 1.5 \pm 0.1\,(sys) \pm 0.7\,(stat)$. The systematic error is estimated compared to the analysis from the two *Planck* y maps. The degeneracy between the density and temperature can be broken using X-ray data. However, the X-ray signal around the superclusters from the *ROSAT* X-ray maps is consistent with zero due to the low sensitivity of X-ray emission in the low-density region.

Assuming a gas temperature of $T_{\rm e} = 8 \times 10^6$ K, estimated in filaments by simulations in Tanimura et al. (2017), we find the total gas mass density associated with our measurement corresponds to $(\Omega_{gas}/\Omega_b)\times(T_{\rm e}/8\times10^6\,{\rm K}) = 0.11 \pm 0.01 \pm 0.05$. Using a higher gas temperature of $kT = 0.91 \pm 0.25$ keV ($T \sim 1.1\times10^7$ K) (gas temperature in a filament estimated from XMM-Newton observations in Werner et al. (2008)), we find $\Omega_{gas}/\Omega_b \simeq 0.08$.

The morphologies and gas distributions of superclusters are complex with their shallow gravitational potentials. Assuming that superclusters are spherically symmetric may underestimate the gas density derived at a given temperature. However, it should not affect the Ω_{gas} value since it is derived from the "total" tSZ signal we measure around the superclusters.

Observational hints were reported that large amounts of WHIM may be encompassed in the crowded environment of superclusters such as PLCK G214.6+37.0, Abell 2199 supercluster and Corona Borealis supercluster. Along with these, our first statistical analysis of the tSZ singal from about 600 superclusters allows us to explore the gas pressure. It allows us to derive, for the first time, the potential contribution of diffuse gas in superclusters to the total baryon budget. To probe such low density regions, a better sensitivity to the tSZ signal would be needed in addition to X-ray data. Moreover, a better understanding of the physical state of the gas in superclusters, especially its temperature, would be required to further identify the diffuse baryon and their contribution. It will be addressed using hydrodynamic simulations on very large scales.

The future LSST (Ivezic et al. 2008; LSST Science Collaboration et al. 2009) and Euclid (Laureijs et al. 2011) data will play an important role in more precise identification of galaxy groups/clusters as well as superclusters. By combining with other surveys, e.g., eROSITA X-ray survey (Merloni et al. 2012) and Sunyaev-Zel'dovich surveys like ACTPpol (Niemack et al. 2010), AdvACT (Henderson et al. 2016) or SPT-3G (Benson et al. 2014) will help unveiling larger quantities of low-density gas in superclusters and to probe its physical properties.

Acknowledgements. This research has been supported by the funding for the ByoPiC project from the European Research Council (ERC) under the European Union's Horizon 2020 research and innovation programme grant agreement ERC-2015-AdG 695561. The authors acknowledge fruitful discussions with the

members of the ByoPiC project (https://byopic.eu/team). We also thank P. Heinamaki and E. Saar for their suggestions.
This publication used observations obtained with /Planck/ (http://www.esa.int/Planck), an ESA science mission with instruments and contributions directly funded by ESA Member States, NASA, and Canada. It made use of the SZ-Cluster Database operated by the Integrated Data and Operation Centre (IDOC) at the Institut d'Astrophysique Spatiale (IAS) under contract with CNES and CNRS. This research has also made use of the VizieR database, operated at CDS, Strasbourg. The publication made use of the community-developed core Phyton package of astropy and numpy/scipy/matplotlib libraries.

References

Araya-Melo, P. A., Reisenegger, A., Meza, A., et al. 2009, MNRAS, 399, 97
Banerjee, P., Szabo, T., Pierpaoli, E., et al. 2018, New A, 58, 61
Basilakos, S. 2003, VizieR Online Data Catalog, 734
Batiste, M. & Batuski, D. J. 2013, MNRAS, 436, 3331
Benson, B. A., Ade, P. A. R., Ahmed, Z., et al. 2014, in Proc. SPIE, Vol. 9153, Millimeter, Submillimeter, and Far-Infrared Detectors and Instrumentation for Astronomy VII, 91531P
Bonjean, V., Aghanim, N., Salomé, P., Douspis, M., & Beelen, A. 2018, A&A, 609, A49
Cen, R. & Ostriker, J. P. 2006, ApJ, 650, 560
Chon, G., Böhringer, H., & Zaroubi, S. 2015, A&A, 575, L14
Chow-Martínez, M., Andernach, H., Caretta, C. A., & Trejo-Alonso, J. J. 2014, MNRAS, 445, 4073
Croston, J. H., Pratt, G. W., Böhringer, H., et al. 2008, A&A, 487, 431
de Graaff, A., Cai, Y.-C., Heymans, C., & Peacock, J. A. 2017, ArXiv e-prints [arXiv:1709.10378]
Einasto, J., Einasto, M., Tago, E., et al. 2007, A&A, 462, 811
Einasto, M., Einasto, J., Tago, E., Müller, V., & Andernach, H. 2001, AJ, 122, 2222
Einasto, M., Liivamägi, L. J., Tago, E., et al. 2011, A&A, 532, A5
Fukugita, M. & Peebles, P. J. E. 2004, ApJ, 616, 643
Henderson, S. W., Allison, R., Austermann, J., et al. 2016, Journal of Low Temperature Physics, 184, 772
Hurier, G., Macías-Pérez, J. F., & Hildebrandt, S. 2013, A&A, 558, A118
Ivezic, Z., Tyson, J. A., Abel, B., et al. 2008, ArXiv e-prints [arXiv:0805.2366]
Jimeno, P., Diego, J.-M., Broadhurst, T., De Martino, I., & Lazkoz, R. 2017, ArXiv e-prints [arXiv:1706.00395]
Kepner, J. & Kim, R. 2000, ArXiv Astrophysics e-prints [astro-ph/0004304]
Laureijs, R., Amiaux, J., Arduini, S., et al. 2011, ArXiv e-prints [arXiv:1110.3193]
Liivamägi, L. J., Tempel, E., & Saar, E. 2012, A&A, 539, A80
LSST Science Collaboration, Abell, P. A., Allison, J., et al. 2009, ArXiv e-prints [arXiv:0912.0201]
Merloni, A., Predehl, P., Becker, W., et al. 2012, ArXiv e-prints [arXiv:1209.3114]
Nicastro, F., Mathur, S., & Elvis, M. 2008, Science, 319, 55
Niemack, M. D., Ade, P. A. R., Aguirre, J., et al. 2010, in Proc. SPIE, Vol. 7741, Millimeter, Submillimeter, and Far-Infrared Detectors and Instrumentation for Astronomy V, 77411S
O'Mill, A. L., Proust, D., Capelato, H. V., et al. 2015, MNRAS, 453, 868
Piffaretti, R., Arnaud, M., Pratt, G. W., Pointecouteau, E., & Melin, J.-B. 2011, A&A, 534, A109
Planck Collaboration, Ade, P. A. R., Aghanim, N., et al. 2014a, A&A, 571, A20
Planck Collaboration, Ade, P. A. R., Aghanim, N., et al. 2014b, A&A, 571, A21
Planck Collaboration, Ade, P. A. R., Aghanim, N., et al. 2013a, A&A, 550, A132
Planck Collaboration, Ade, P. A. R., Aghanim, N., et al. 2013b, A&A, 550, A134
Planck Collaboration, Ade, P. A. R., Aghanim, N., et al. 2011a, A&A, 536, A8
Planck Collaboration, Ade, P. A. R., Aghanim, N., et al. 2016a, A&A, 594, A27
Planck Collaboration, Ade, P. A. R., Aghanim, N., et al. 2016b, A&A, 594, A13
Planck Collaboration, Ade, P. A. R., Aghanim, N., et al. 2016c, A&A, 594, A24
Planck Collaboration, Aghanim, N., Arnaud, M., et al. 2011b, A&A, 536, A9
Planck Collaboration, Aghanim, N., Arnaud, M., et al. 2016d, A&A, 594, A22
Pratt, G. W., Croston, J. H., Arnaud, M., & Böhringer, H. 2009, A&A, 498, 361
Proust, D., Quintana, H., Carrasco, E. R., et al. 2006, A&A, 447, 133
Rauch, M., Miralda-Escudé, J., Sargent, W. L. W., et al. 1997, ApJ, 489, 7
Reisenegger, A., Quintana, H., Carrasco, E. R., & Maze, J. 2000, AJ, 120, 523
Remazeilles, M., Aghanim, N., & Douspis, M. 2013, MNRAS, 430, 370
Rines, K., Mahdavi, A., Geller, M. J., et al. 2001, ApJ, 555, 558
Rykoff, E. S., Rozo, E., Busha, M. T., et al. 2014, ApJ, 785, 104
Shull, J. M., Smith, B. D., & Danforth, C. W. 2012, ApJ, 759, 23
Sunyaev, R. A. & Zeldovich, I. B. 1980, ARA&A, 18, 537
Sunyaev, R. A. & Zeldovich, Y. B. 1970, Ap&SS, 7, 3
Sunyaev, R. A. & Zeldovich, Y. B. 1972, Comments on Astrophysics and Space Physics, 4, 173
Tago, E., Saar, E., Tempel, E., et al. 2010, A&A, 514, A102
Tanimura, H., Hinshaw, G., McCarthy, I. G., et al. 2017, ArXiv e-prints [arXiv:1709.05024]
Weinberg, D. H., Miralda-Escudé, J., Hernquist, L., & Katz, N. 1997, ApJ, 490, 564
Wen, Z. L. & Han, J. L. 2015, ApJ, 807, 178
Wen, Z. L., Han, J. L., & Liu, F. S. 2012, ApJS, 199, 34
Werner, N., Finoguenov, A., Kaastra, J. S., et al. 2008, A&A, 482, L29
Yao, Y., Shull, J. M., Wang, Q. D., & Cash, W. 2012, ApJ, 746, 166
Zeldovich, I. B., Einasto, J., & Shandarin, S. F. 1982, Nature, 300, 407
Zeldovich, Y. B. & Sunyaev, R. A. 1969, Ap&SS, 4, 301